JOURNAL OF MATERIALS SCIENCE **40** (2005) 1731–1741

Mechanical behaviour of a solid with many stress corrosion growing cracks

F. LE POULAIN, M. TOUZET, M. PUIGGALI, I. AUBERT
Laboratoire de Mécanique Physique, UMR 5469 CNRS, Université Bordeaux 1, 351 Cours de la Libération, 33405 Talence Cedex, France

The theory of effective elastic properties of cracked solids is used to predict the degradation of mechanical properties of a stainless steel induced by stress corrosion growing cracks. The material is considered as an evolutionary composite with a cracked external volume (damaged elastic behaviour) and a safe internal volume (elastoplastic behaviour). From continuous surface observation of cracks by in situ videomicroscopy, the influence of interactions between multiple cracks is particularly studied. We show that coalescence of cracks can be neglected and that amplification and shielding effects counterbalance each other. This experimental study allows to choose the most suitable method to determine the effective elastic properties. Then, we propose a modelling to represent the overall mechanical behaviour of a solid with many surface cracks. Simulated and experimental slow strain rate curves are compared.

1. Introduction

Small surface cracks are commonly observed in fatigue, fatigue corrosion (FC) and stress corrosion cracking (SCC). These crack colonies, nucleating on the surface and propagating both on the surface and into the bulk of the material, lead to the final fracture. In this case, predicting and evaluating the structural safety is a complex process since crack interactions can occur. A great deal of research work has been centered around this problem.

Among the existing ways, experimental approaches have been favoured in SCC and FC studies. The next section will review some methods used in SCC and FC studies to predict the failure of a structure when interactions between cracks are considered.

Another way to predict the overall degradation of cracked solids is to determine the effective elastic properties by a theoretical approach. These studies will be presented and particularly focused on the effect of interaction on effective properties, since the objective of this paper is to apply the effective media theory to a material with stress corrosion growing cracks.

1.1. Review of SCC, FC and fatigue studies on interacting growing cracks

The main purpose of SCC and FC studies concerning solids with many surface cracks is to predict the remaining life of the structure. This objective is very difficult to reach due to interactions between cracks. These interactions can produce two antagonistic effects—stress shielding and stress amplification [1–3]—leading either to deceleration or acceleration in crack growth, both depending on crack lengths and relative positions.

In order to analyse these interaction effects, many experimental studies have been performed to estimate crack growth rates and evaluate time to failure. The same approach has been favoured by the authors [4–9] i.e., characterizing crack growth behaviour on the surface by means of fatigue tests or fatigue corrosion tests. Each test was interrupted at appropriate intervals and microscopic examinations were carried out to obtain the length and the location of cracks on the surface. Sometimes, when crack density was high, interactions between crack tips due to the stress amplification could lead to coalescence. So, criteria for coalescence had to be defined [6]. Among the most useful criteria, the Ochi [10] criterion was frequently chosen; it depends on the crack lengths and the distance between crack tips. When the coalescence criterion is satisfied, both cracks are recharacterized as a single crack. These authors also show that cracks can cease to grow when other large cracks located in their neighbourhood can induce a stress shielding effect.

Then, the stochastic behaviour of SC cracks led the authors to consider a statistical and/or a probabilistic approach to simulate the whole process of crack growth [5, 6, 8]. These authors have shown that there is a good agreement between predicted and experimental results—more particularly as concerns the time before the critical crack length on the surface.

However, these problems are three-dimensional in nature and surface analysis is not sufficient since material degradation is considerably influenced by in-depth propagation. Stolarz [11] has shown that surface crack coalescence does not affect the in-depth kinetics of the fatal crack. Santarini [12] has shown that cracks are deeper than longer by using several specimens progressively sectioned to obtain crack profiles. Wang *et al.*

[8] explain that crack propagation generally occurs to a greater extent along the surface than in depth, promoting length-depth ratios of about 4 for a Mn-Cr steel. This paper will discuss the influence of crack interaction on crack growth both on surface and depth.

1.2. Effective elastic properties of solids with many cracks

Another way for studying the effect of many cracks on material degradation consists in determining the effective elastic properties since there is no exact solution to this problem. A great amount of approximate schemes has thus been developed. We can distinguish two main approaches which integrate or not crack interactions:

– The non-interacting approximation was developed by Kachanov [2]. Each crack is considered as an isolated one and is subjected to an applied stress σ. The author considers that both interaction effects (shielding and amplification) may be neglected due to the competition between them.

– The homogenization methods take into account crack interactions. These approaches are based on micro-macro scale transition and allow to determine the effective elastic properties from the microscopic behaviour scale. A superposition of elementary problems is treated, each one is composed of one crack surrounded by an effective environment. There are two main groups of approximate schemes: the methods of effective matrix where each crack is embedded in a matrix of reduced stiffness (self-consistent scheme [13, 14], differential scheme [15, 16]) and the methods of effective field where a representative crack is placed in the undamaged matrix and loaded with an effective stress field (method of Mori-Tanaka [17]). In the methods of effective matrix, crack interactions are predicted to always reduce the effective stiffness, compared to that calculated with the interactions neglected [2]. Thus, the stiffening impact of the shielding interactions is ignored. In the methods of effective field, the shielding mode of interactions is not disregarded and in the simplest version (Mori-Tanaka), the results coincide with the method of non-interacting cracks when cracks are randomly located. Carvalho *et al.* [18] compared all these methods by confronting them with experimental results. They observed that the non-interacting approximation gave the best results as the competing effects of the interactions counterbalance each other.

The objective of this paper is to present a modelling of the mechanical behaviour degradation of a material with stress corrosion cracks. Experimental results are presented in order both to obtain experimental data and to discuss the method chosen to determine the effective elastic properties. Then simulated and experimental results are compared.

2. Experiments

To obtain quantitative characterization of the evolution of surface cracks, slow strain rate tests (SSRT) were performed using 304L stainless steel in Scheil reagent (boiling 44% $MgCl_2$ solution at 153°C).

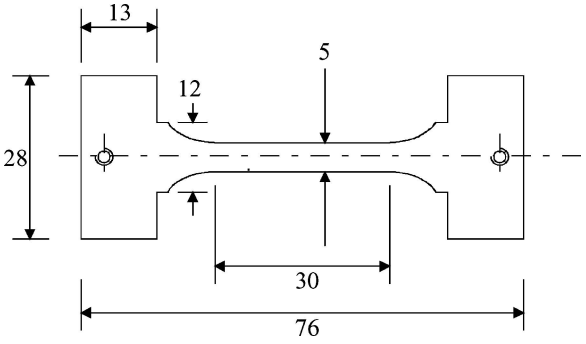

Figure 1 Test specimen (mm) (thickness 2 mm).

2.1. Experimental method

Tension specimens (Fig. 1) were machined from plates of 304L stainless steel by laser cutting. The calibrated zone was 30 mm long, 5 mm wide and 2 mm thick. Specimens were annealed at 1050°C for 30 min, water quenched and then electropolished in anhydrous perchloric acid followed by an acid etching to identify grain boundaries. The chemical composition of the steel is presented in Table I.

The mechanical behaviour was described by the Ramberg-Osgood law which is commonly used to represent the monotonic stress-strain curves for stainless steels:

$$\begin{cases} \sigma = E\varepsilon^e & \text{if } \sigma < \sigma_y \\ \sigma = \sigma_y + k(\varepsilon^p)^n & \text{if } \sigma \geq \sigma_y \end{cases} \quad (1)$$

with $\sigma, \varepsilon^e, \varepsilon^p$ the stress, the elastic strain, the plastic strain in the tensile direction, σ_y the yield stress, E the Young modulus of the isotropic material, k and n the parameters of the Ramberg-Osgood law. These parameters obtained from a SSRT (strain rate $\dot{\varepsilon} = 6.4 \times 10^{-6}\,s^{-1}$) in silicone oil at 153°C are presented in Table II.

Specimens were immersed in Scheil reagent for 2 h (until potential stabilization) before SSRT were performed at strain rates between 3.2×10^{-6} s^{-1} and 8×10^{-6} s^{-1}. Damage modifications were followed by in-situ optical video-microscopy [19].

In-situ observations through a corrosion cell with a CCD camera were performed in order to characterize quantitatively changes in each surface crack length and crack location. The CCD camera was assembled on a 3D micrometric displacement system and connected to a computer to take VGA format images (640 × 480 pixels). A part of the gauge surface was explored (6 to

TABLE I Chemical composition of test material (wt.%)

Element	C	Cr	Ni	Si	Mn	S	P
Composition	0.02	18.18	10.05	0.66	1.44	0.007	0.026

TABLE II Mechanical properties of test material

E	υ	σ_y	k	n
193 GPa	0.3	105 MPa	1244 MPa	0.86

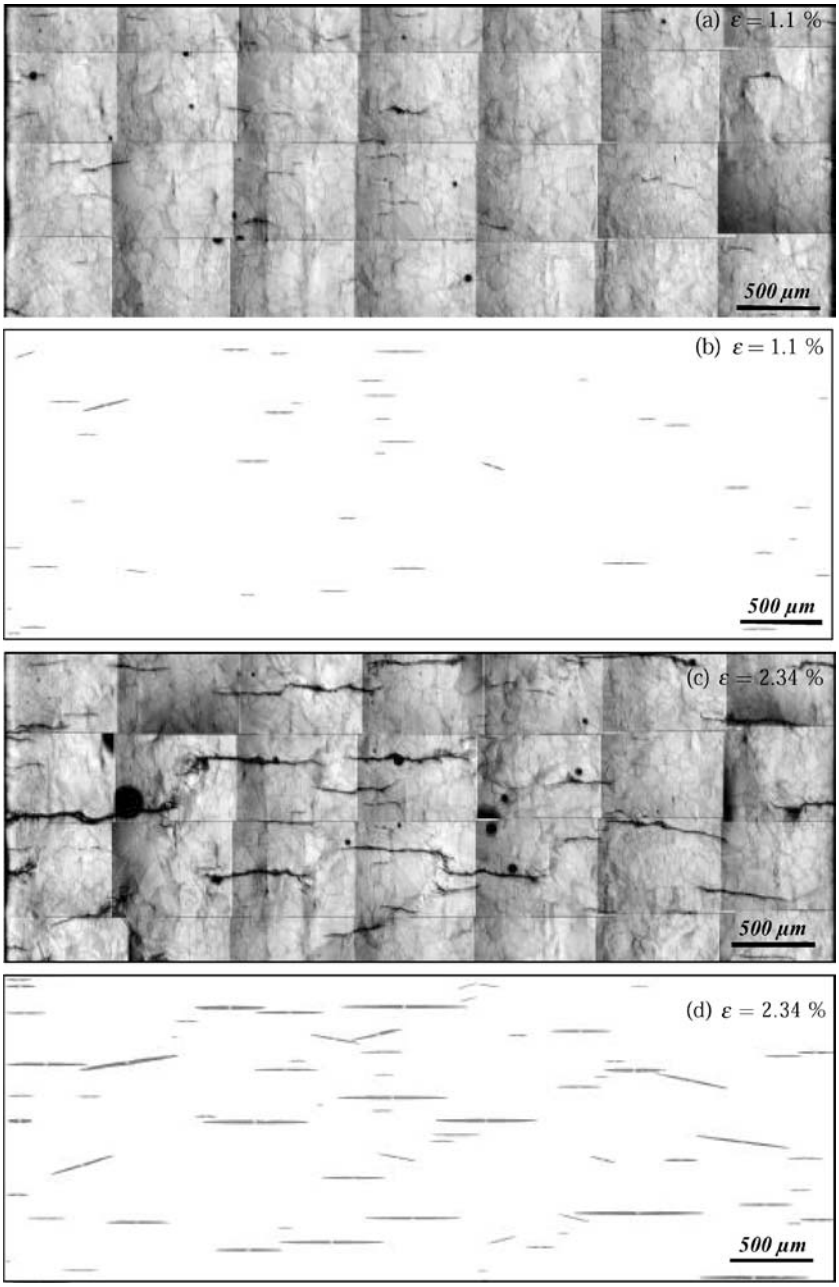

Figure 2 In-situ surface observations for various strain level (SSRT test at $\dot{\varepsilon} = 6.4 \times 10^{-6}$ s^{-1}). (a) and (c): rebuilt images; (b) and (d): binary images.

7%), which corresponds to 8 to 10 mm^2 and 28 images for a magnification of 270. Surface imaging was carried out throughout the test. The images were assembled with an image processing software in order to provide a single image (Fig. 2a and c). Maps of crack distribution were obtained with the Scion Image Beta 4.02 software (Scion Corporation) for each reconstitution (Fig. 2b and d). For each map, we obtained the number, the length, the opening and the position of the cracks.

2.2. Experimental results

This part presents results obtained for three SSRT: $\dot{\varepsilon} = 3.2 \times 10^{-6}$ s^{-1}, $\dot{\varepsilon} = 6.4 \times 10^{-6}$ s^{-1} and $\dot{\varepsilon} = 8 \times 10^{-6}$ s^{-1}. These strain rates belong to the range of SCC sensitivity. For this material-media system, beyond a strain rate of 10^{-5} s^{-1}, cracks remain very short and slow strain rate curves are quite similar in corrosive and inert media. For strain rates below 10^{-6} s^{-1}, very few isolated cracks are observed.

Fig. 3 shows slow strain rate curves in both inert and corrosive media at the same temperature. The SCC results obtained are classical i.e., there is no modification in the elastic range and we observe a loss of mechanical properties in corrosive media, degradation enhanced with the decrease of the strain rate.

Fig. 4 displays experimental and simulated crack density versus strain for three strain rates. Even though the number of cracks depends on strain rate, three stages are observed in each test: initial, intermediate and final, corresponding to changes in nucleation rate. It can be noted that the number of cracks increases very progressively, then presents a linear tendency until it reaches a saturation value after the maximum strength whatever the strain rate. To take into account the progressive nucleation of the cracks and the saturation phenomenon in

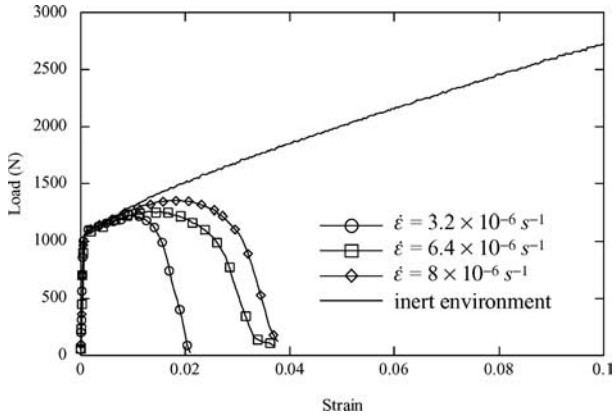

Figure 3 Slow strain rate curves of 304L stainless steel in boiling $MgCl_2$ for three strain rates and in inert environment (oil silicone) at 153°C.

crack density observed at the end of the test, we chose to simulate the evolution of crack density by a law based on the two-parameter Weibull law:

$$N(\varepsilon) = N_{\text{inf}} F(\varepsilon) = N_{\text{inf}}\left(1 - e^{-\left(\frac{\varepsilon}{\eta}\right)^{\beta}}\right) \qquad (2)$$

in which β is the shape parameter, η is the scale parameter and N_{inf} is the total crack density at the end of the test. The identification of these parameters was carried out numerically. The results of crack initiation simulation are presented in Fig. 4 and they show a good agreement of this law based on a Weibull distribution with the experimental density of cracks.

The following paragraphs present an analysis of crack propagation during these three nucleation stages.

2.2.1. Initial stage

Initial cracks nucleate mainly in large-size grains where micro plasticity is observed. Few cracks are stopped by grain boundaries. Crack distribution is homogeneous and since crack density is low, no interactions are observed (Fig. 5).

2.2.2. Intermediate stage

We noted both an increase in crack initiation and in collective crack growth. However, the propagation rate may vary depending on the interactions generated by the relative positions of the cracks with a negligible effect of the microstructure due to crack size (larger than the grain size). To demonstrate the effect of interactions on crack propagation, we compared the lengths of the cracks to the average crack length (ratio between cumulated length and crack number) for three crack configurations:

- *Isolated cracks (Fig. 6a)*
  In this case, the length of isolated cracks presents the same evolution as the average crack length. We observe a stop or a deceleration of these isolated cracks just after maximum strength (final stage).
- *Stacked cracks (Fig. 6b)*
  Apart from the end of the test, the behaviour of the longest crack (crack 1) is relatively similar to the average crack. Crack 1 behaves like an isolated crack. Crack 2 has a lower growth rate although it started at the same time. This deceleration in growth rate is due to the shielding effect induced by the longest crack. If cracks are stacked, the shielding effect constitutes the only interaction effect.

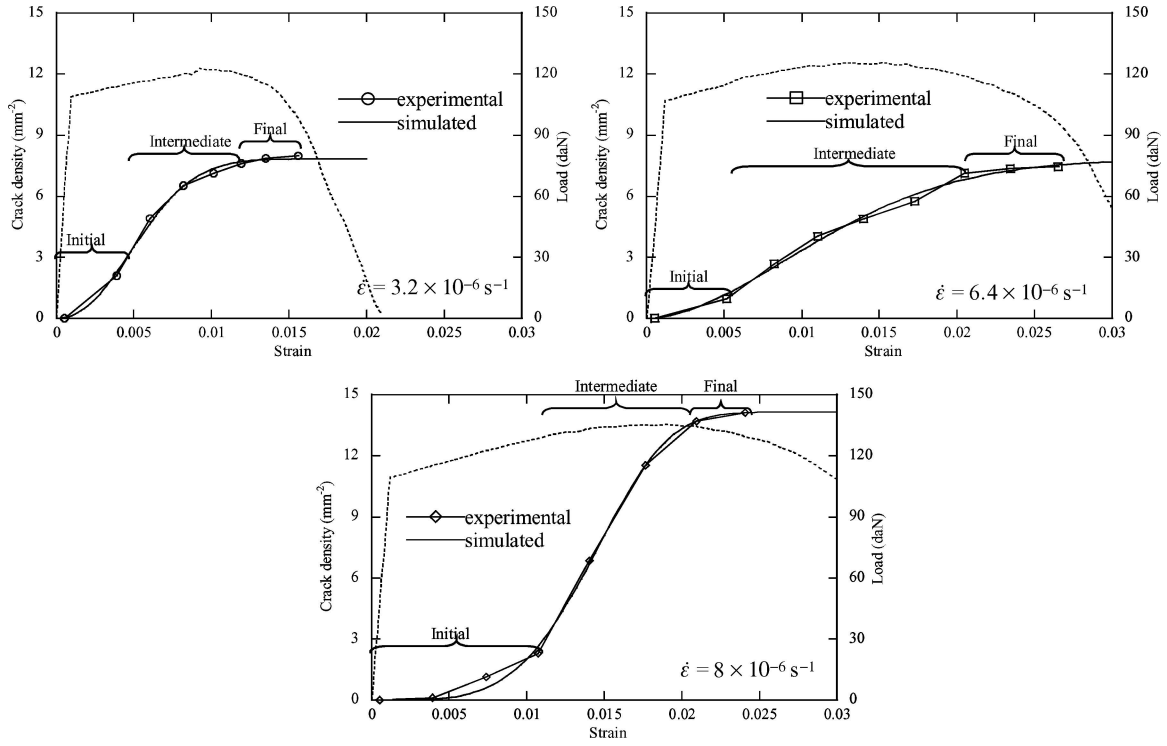

Figure 4 Experimental and simulated crack density and load versus strain: three stages of crack density evolution.

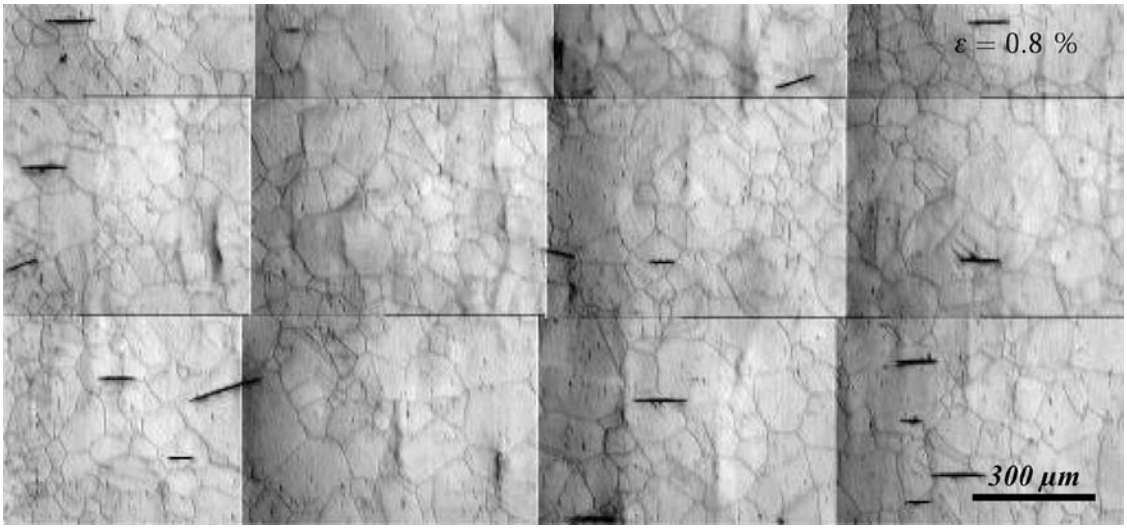

Figure 5 $\dot{\varepsilon} = 6.4 \times 10^{-6}\ s^{-1}$. The location of the first initiated cracks is homogeneous.

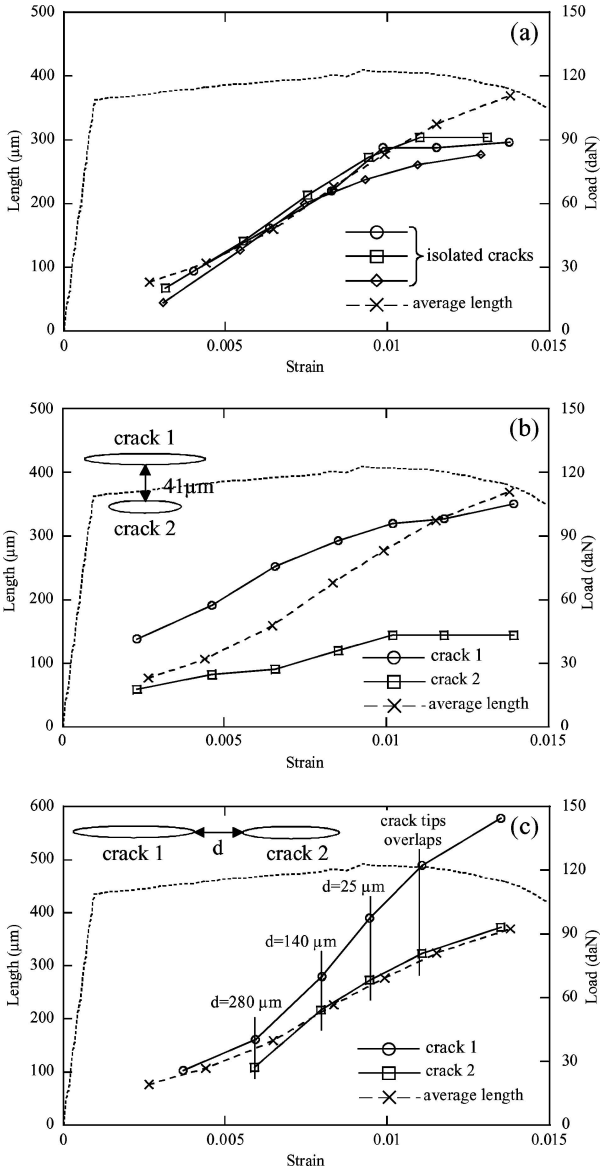

Figure 6 Comparison of some crack lengths with the average crack length for three crack configurations at $\dot{\varepsilon} = 3.2 \times 10^{-6}\ s^{-1}$. a: isolated cracks, b: stacked cracks, c: aligned cracks.

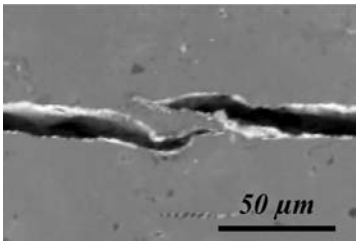

Figure 7 The meeting of the crack tips: deviation of the inner crack tips. $\varepsilon = 2.2\%$, $\dot{\varepsilon} = 6.4 \times 10^{-6}\ s^{-1}$.

- *Aligned cracks (Fig. 6c)*
  If cracks are aligned, the growth rate of the longest crack is higher than that of the average crack. This configuration induces an amplification effect of growth rate. When inner crack tips become very close, we observe that crack tips tend to deviate past each other to overlap in the plastic zone of the two crack tips (Fig. 7). In this stage, we do not observe the tear of the plastic ligament between the crack tips, so the meeting of the crack tips does not lead to coalescence of cracks.

During the intermediate propagation stage, when crack density increases linearly, we observe both types of interactions which depend on crack lengths and relative positions. The latter change and the interactions are modified since the cracks propagate. In this stage, although interactions between crack tips exist, coalescence between long cracks is never observed. When it occurs, it is always related to the joining of a macro-crack with a micro-crack nucleated in the plastic zone developed at the macro-crack tip. This process does not modify the macro-crack propagation rate.

2.2.3. Final stage

After the maximum strength, we classically observe the stop or the deceleration of a lot of cracks. In this stage, we clearly see the tear of the plastic ligament between adjacent crack tips (Fig. 8). In this particular case, the

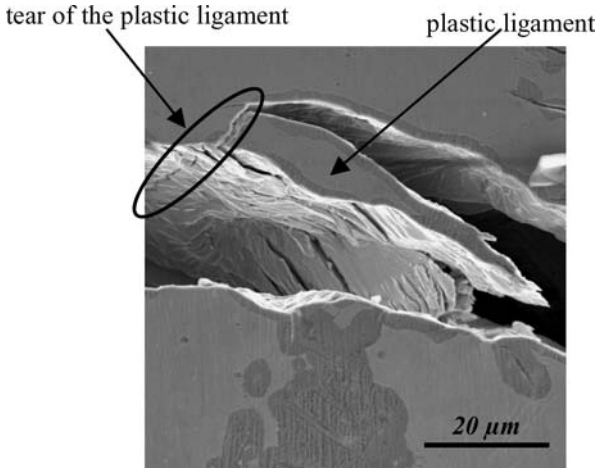

Figure 8 Tear of the plastic ligament between adjacent crack tips which induces crack coalescence at the end of the test (final stage).

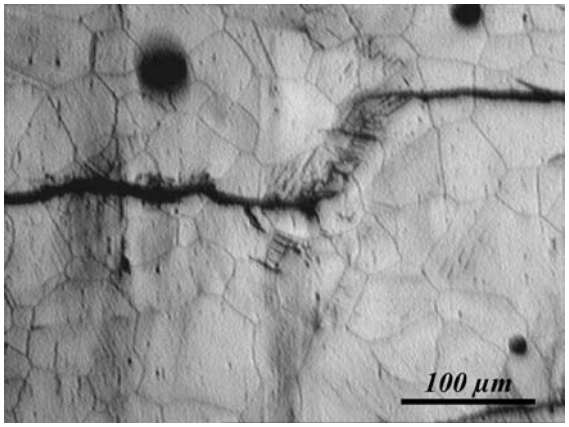

Figure 9 $\dot{\varepsilon} = 6.4 \times 10^{-6}\ s^{-1}$, $\varepsilon = 2.65\%$ interaction zones between macroscopic cracks.

coalescence of few macroscopic cracks induces a stress shielding effect on the others. A saturation of the crack density occurs and the last created defects are localized in the interaction zones between macroscopic cracks (Fig. 9). Coalescence of some neighbouring long cracks may be the failure criterion at this stage.

Interactions between surface cracks are often observed and begin early in the test. These interactions can lead to a decrease of the crack growth rate for stacked cracks and an increase of the crack growth rate when cracks are aligned.

Nevertheless, coalescence of macro-cracks i.e., when two cracks are recharacterized as a single crack was never encountered apart from the end of the test. This phenomenon can be explained because when crack tips overlap, then they are no longer in the same plane. Fig. 10 shows propagation in depth of three cracks and even if at the end of the test ductile ligament between crack is broken, this ligament exists on all the depth of each crack.

These observations have provided the basic hypotheses for the model presented now.

3. Modelling

Classical fractographic observations in SCC studies (Fig. 11) show two distinct zones: a cleavage-like area due to brittle SC cracks on the outer surface

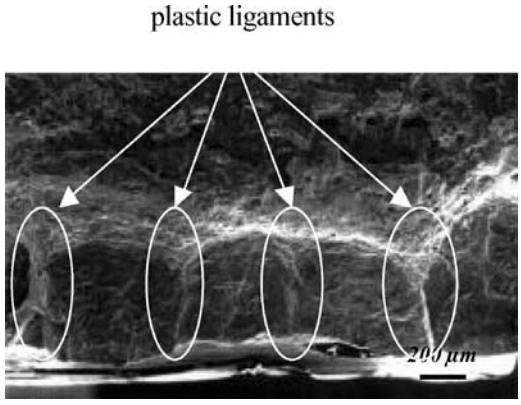

Figure 10 SEM of fracture surface showing that surface coalescence has not impact on propagation in depth. SSRT performed at $\dot{\varepsilon} = 6.4 \times 10^{-6}\ s^{-1}$, interrupted at $\varepsilon = 2.2\%$ and then broken in air.

and a purely ductile zone (with dimples) in the inner part of the specimen. The ductile area is similar to the fracture surface observed in inert media. The external zone with many crystallographic cracks is an indication of weak plastic deformation. Surface observations also show that plasticity remains mainly localized around crack tips. Moreover, we observe an irreversible opening of the cracks (Fig. 12) which is the result of the plastic deformation of the inner part. So, we can reasonably consider that the material preserves an overall damaged elastic behaviour on the external surface.

These observations allow to consider the sample as a bi-material (Fig. 13) with an inner ductile volume (elastoplastic behaviour) and an outer cracked volume (damaged elastic behaviour). As the damage progresses in depth, the ratio of these two parts is modified during the test.

It is necessary to specify the field of validity of our model. We noted in our experiments that there was a collective behaviour of the cracks in the initial and intermediate stages. So, the model cannot describe localized phenomena observed at the end of the test.

In the equations developed below, the parameters relative to the safe volume are marked s and those relative to the cracked volume are noted c.

The behaviour of the non-cracked volume is described by the Ramberg-Osgood law (Equation 1).

For the external cracked volume, considering a uniaxial applied stress σ^c, we have:

$$\sigma^c = E^* \varepsilon^{ec} \tag{3}$$

with ε^{ec} the elastic strain and E^* the longitudinal effective Young modulus. We consider the longitudinal strain continuity between the safe volume and the cracked volume:

$$\varepsilon = \varepsilon^s = \varepsilon^c = (\varepsilon^{es} + \varepsilon^{ps}) = (\varepsilon^{ec} + \varepsilon^{inel}) \tag{4}$$

- with the strain of the safe part $\varepsilon^s = (\varepsilon^{es} + \varepsilon^{ps})$, ε^{es} and ε^{ps} are respectively the elastic and plastic strains,

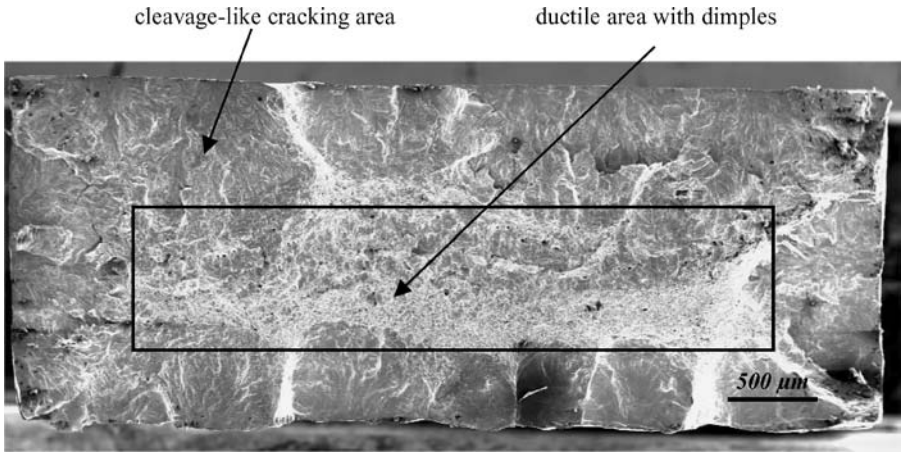

Figure 11 SEM of fracture surface of 304L stainless steel in boiling $MgCl_2$ at 153°C after a SSRT ($\dot{\varepsilon} = 6.4 \times 10^{-6}$ s^{-1}) interrupted at $\varepsilon = 2.2\%$ and then broken in air showing cleavage-like cracking on the external contour and ductile dimpled fracture in the center.

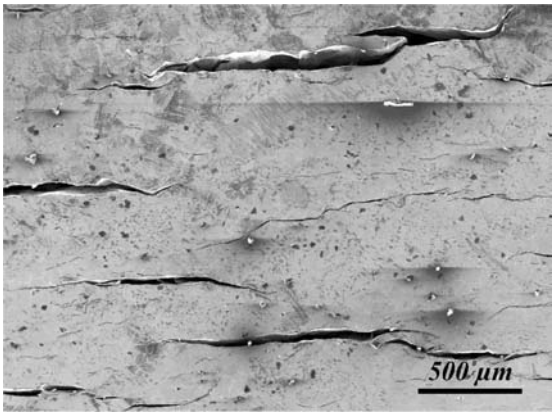

Figure 12 SEM showing an irreversible opening of the cracks on the external surface after a slow strain rate test performed at $\dot{\varepsilon} = 6.4 \times 10^{-6}$ s^{-1}.

- with the strain of the cracked part $\varepsilon^{c} = (\varepsilon^{ec} + \varepsilon^{inel})$, ε^{ec} is the elastic strain, and ε^{inel} the strain due to the irreversible opening of cracks on the external surface induced by the plastic deformation of the internal volume.

From equilibrium considerations, F, the load acting on the overall specimen is given by:

$$F = F^{s} + F^{c} \tag{5}$$

in which F^{c} and F^{s} are respectively the loads applied to the cracked and the safe parts. The corresponding stress σ (i.e., $\sigma = F/S$) according to the total strain ε of the material can be expressed by:

$$\sigma = \frac{S^{c}}{S} E^{*}(\varepsilon - \varepsilon^{inel}) + \frac{S^{s}}{S}\left(\sigma_{y} + k\left(\varepsilon - \frac{S\sigma - S^{c}E^{*}(\varepsilon - \varepsilon^{inel})}{S^{s}E}\right)^{n}\right) \tag{6}$$

with S^{s}, S^{c}, $S = (S^{s} + S^{c})$, respectively the sections of the safe volume, the cracked volume and the overall specimen. Now, we have to determine:

- the effective elastic properties of the cracked volume, characterized by E^{*},

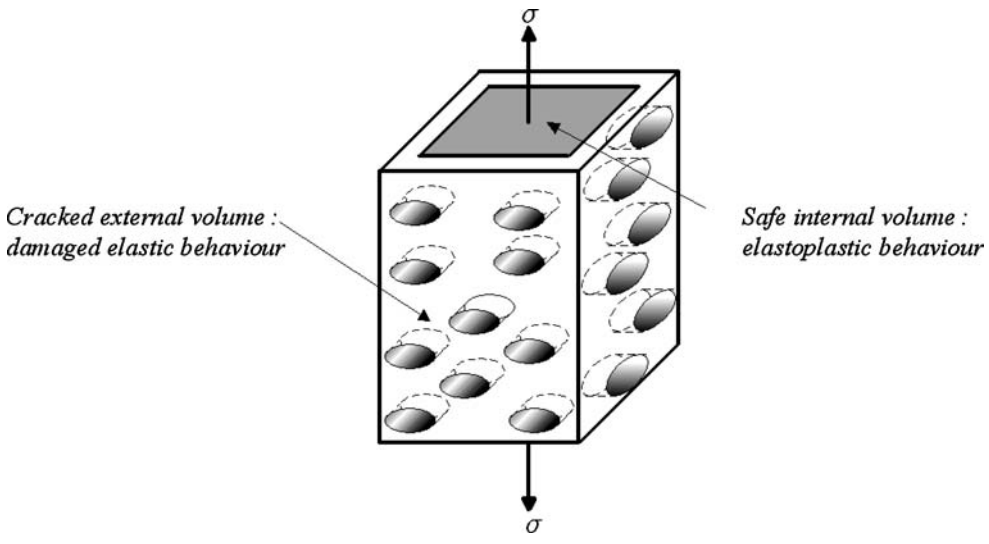

Figure 13 Material considered as an evolutionary composite with a cracked external volume with elliptic holes (damaged elastic behaviour) and a safe internal volume (elastoplastic behaviour).

- the inelastic strain $\varepsilon^{\text{inel}}$,
- the ratio between the sections of the safe part S^{s} and the cracked part S^{c}.

3.1. Effective elastic properties: Determination of E^*

In order to find the most suitable method, we refer to our analysis on interaction between cracks. In the field of validity of our model, we showed that no interactions occur in the initial stage. Then, in the intermediate stage, both shielding and amplification effects are present and we can consider that the competing effect of the interactions counterbalance each other. So, we use the approximation of non-interacting cracks developed by Kachanov [2] to determine the effective elastic properties.

To take into account the irreversible opening, the cracks are modelled by elliptic holes. The cracked part is represented by a two dimensional elastic material perforated by N parallel elliptic holes (Fig. 13). A closed form of the effective longitudinal Young modulus [20] is given by:

$$E^* = E(1 + p + 2\rho)^{-1} \tag{7}$$

where p is the porosity of material and ρ is the crack density parameter defined in the following way:

$$p = \frac{\pi}{A}\sum_{i=1}^{N} a_i b_i \quad \text{and} \quad \rho = \frac{\pi}{A}\sum_{i=1}^{N} a_i^2 \tag{8}$$

with a_i and b_i respectively the half-length and the half-opening of the crack i, N the total number of cracks on a given area A.

3.2. Inelastic strain: $\varepsilon^{\text{inel}}$

The inelastic strain can be obtained from the Equation 4:

$$\varepsilon^{\text{inel}} = \varepsilon - \varepsilon^{\text{ec}} \tag{9}$$

According to Kachanov [2], the elastic strain ε^{ec} is the sum of two terms:

- a regular one ε^0,
- an additional strain $\Delta\varepsilon$ due to reversible crack opening in linear elasticity.

We assume that between cracks the material preserves an overall elastic behaviour on external surface. So, the regular term $\varepsilon^0 = \sigma^{\text{c}}/E$ is the elastic strain reached at the end of the elastic domain during SSRT:

$$\varepsilon^0 = \frac{\sigma_{\text{y}}}{E} \tag{10}$$

The additional strain due to the presence of the holes ε is written [2]:

$$\Delta\varepsilon = \frac{\sigma^{\text{c}}}{E}(p + 2\rho) \tag{11}$$

Since between cracks, the elastic strain cannot exceed the strain reached at the yield stress, the stress in the cracked part is bounded by $\sigma^{\text{c}} = E^*\varepsilon^0$. According to the Equations 9, 10 and 11 the inelastic strain is expressed:

$$\varepsilon^{\text{inel}} = \varepsilon - \frac{\sigma_{\text{y}}}{E}\left(1 + \frac{E^*}{E}(p + 2\rho)\right) \tag{12}$$

3.3. Evolution of the proportion of safe part S^{s} and cracked part S^{c}

Our experimental investigations have allowed to determine the lengths of cracks on the surface, so we need to evaluate their depths to estimate the cracked part S^{c}. We use the results of Peyrat *et al.* [21] who characterize the shape of cracks for the same material-environment system and during SSRT. This work has shown that the propagation in depth of the cracks was dependent on their propagation on the surface. The authors have established the following relation between surface length and depth:

$$a_{\text{i}} = \alpha c_{\text{i}} + a_{\text{wi}} \tag{13}$$

with a_{i} the half surface length and c_{i} the depth of the crack i, α is the parameter which characterizes the surface/depth dependence and a_{wi} is the initial half-length. Peyrat has shown that the parameters α and a_{wi} can be considered constant during the test ($\alpha = 0.45$ and $a_{\text{wi}} = 1.29$ μm). We assume this linear dependence between length and depth and we apply this relation both to the average crack and to a representative crack. The latter is obtained from Equation 8 in the following way:

$$a_{\text{rep}}^2 = \frac{1}{N}\frac{A\rho}{\pi} = \frac{1}{N}\sum_{i=1}^{N} a_{\text{i}}^2 \tag{14}$$

In the next section, we will discuss the effect of both average crack and representative crack on simulated curves.

4. Simulation and discussion

Figs 14 and 15 present the changes in porosity p and in crack density parameter ρ for three strain rates. All the evolutions have been simulated by power laws. Both simulated parameters are in good agreement with experimental results except at the end of the test (final stage). In this part of the test, simulation overestimates porosity and crack density parameter since few long cracks propagate.

The results of simulations are presented in Fig. 16. They display:

- the experimental curves (inert and corrosive media),
- the simulated curves obtained with both the average crack and the representative crack,
- the contribution of the cracked part and the safe part estimated with the representative crack.

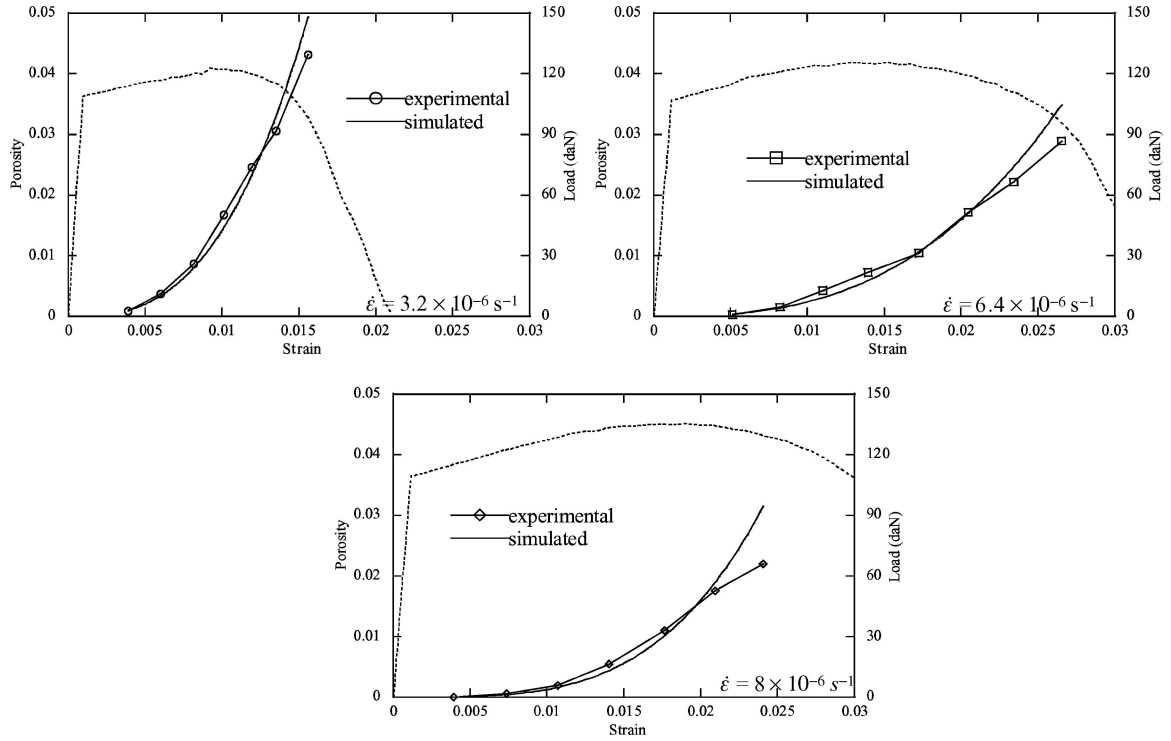

Figure 14 Evolution of porosity p versus strain for three strain rates.

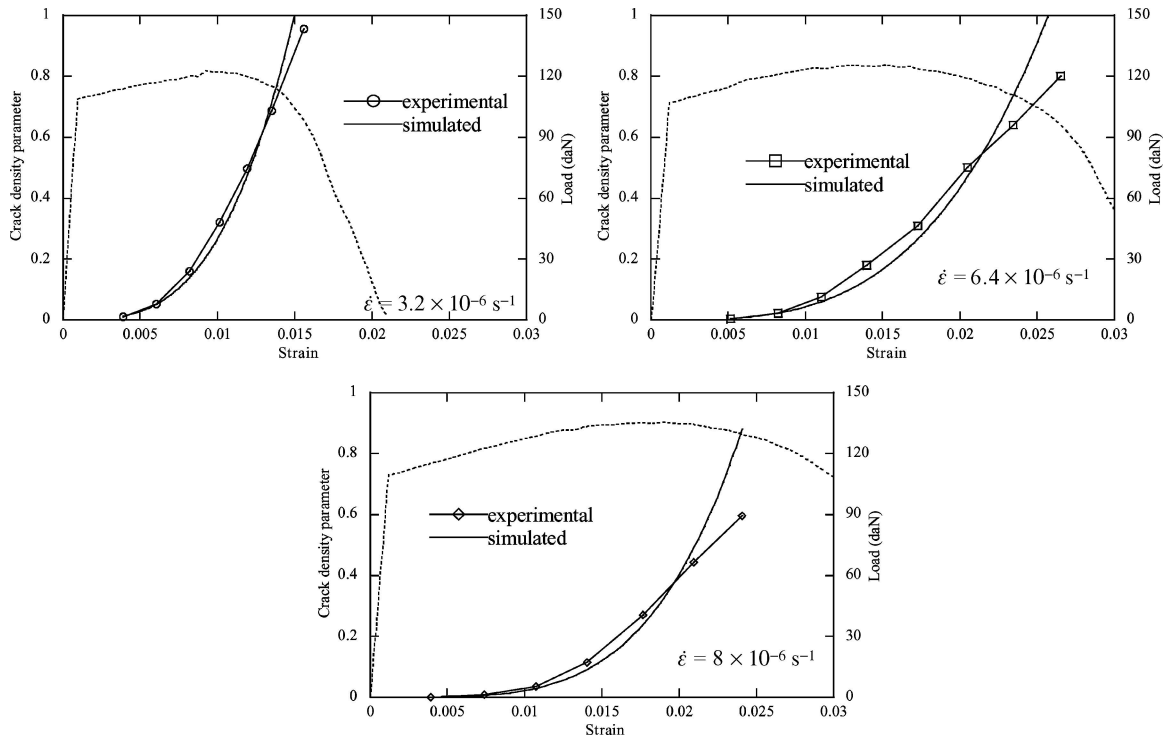

Figure 15 Evolution of the crack density parameter ρ versus strain for three strain rates.

The results of simulations of the overall behaviour are always in good agreement with the experimental curves. Therefore, the choice of an evolutionary bi-material with an inner ductile volume and an outer cracked volume is suitable to represent the overall mechanical behaviour of a solid with many surface cracks.

Simulated curves with the representative crack are slightly below the curves obtained with the average crack. This result is due to the dominating effect of the longest cracks obtained with the representative crack. However, in this case, this effect is not significant. It points to an homogeneous distribution of crack lengths close to the average length.

The contributions of the cracked and safe parts are due to the following competing effects:

- For the cracked part, the decrease of the elastic properties and the increase of the cracked section. At the beginning of the test, the major effect is

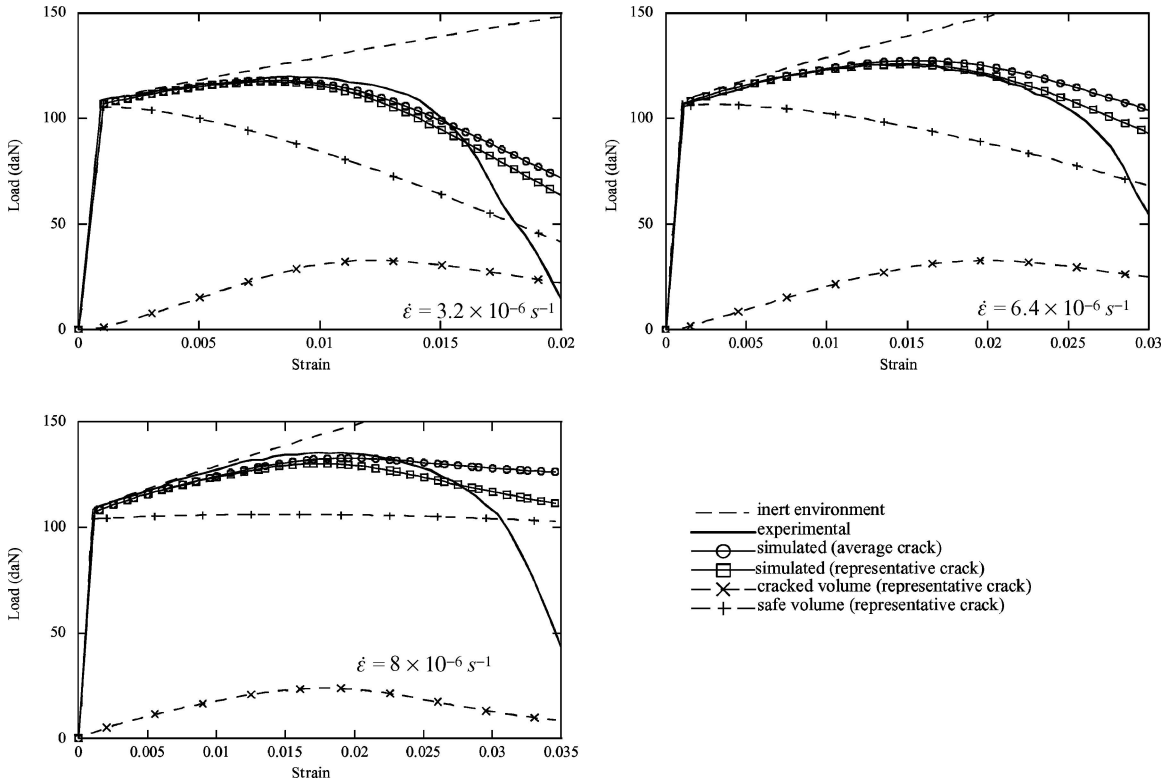

Figure 16 Confrontation between simulated curves and experimental curves for three strain rates.

due to the increase of S^c. Then, the decrease of the elastic properties becomes prevalent.

- For the safe part, the decrease of the safe section and the work hardening. The decrease of the safe section S^s has a major effect except for $\dot{\varepsilon} = 8 \times 10^{-6}\ s^{-1}$ in which the competing effects counterbalance each other.

5. Conclusion

The theory of effective elastic properties of solids containing many cracks was applied to surface SCC. Experimental results allowed to choose—from existing models—the most suitable for predicting changes of the mechanical behaviour of a stainless steel in hot chloride media.

Experimental results show that:

- Crack initiation occurs continuously during all the tests.
- Interactions between cracks are often observed. Both increase and decrease of crack growth rates are linked to crack locations inducing stress amplification and stress shielding. These interactions change during the entire test because crack configurations are continuously modified by propagation.
- During the major part of the test, when coalescence occurs (i.e., when two cracks become a single one), it is always related to the joining of a macro-crack with a micro-crack nucleated in the crack tip plastic zone of the macro-crack. This process does not modify crack propagation rate of the macro-crack. This phenomenon is not the main driving force of crack propagation during the greatest part of the test.
- Coalescence of few long cracks is only observed at the end of the test.

The theory of effective elastic properties is always applied to a structure with non-propagating cracks. The choice of a theoretical model taking interactions into account depends on the kind of interactions that are favoured. Our experimental results allowed to show that neither amplification nor shielding effects dominate the propagation of cracks. The non-interacting cracks theory proposed by Kachanov was used to describe the mechanical behaviour of the external cracked volume. To compare experimental results and theoretical study, the material was considered as an evolutionary bi-material (with an external damaged volume associated with an internal ductile volume). A good agreement was obtained between simulated and experimental mechanical behaviour. Our model deliberately discarded coalescence of cracks because we have showed that it is not the main driving force of damage evolution in depth except at the end of the test. Considering coalescence—i.e., when two cracks are recharacterized as a single crack—would mean a resulting crack depth higher than the crack depth of each crack, and would thus lead to underestimating the macroscopic mechanical behaviour. However, a criterion of coalescence between long cracks could be included in the model to predict the final fracture.

References

1. M. HORI and S. NEMAT-NASSER, *J. Mech. Phys. Solids* **35**(5) (1987) 601.

2. M. KACHANOV, in "Advances in Applied Mechanics," edited by J. W. Hutchinson and T. Y. Wu (Academic Press, New York, 1993) p. 259.
3. M. KAMAYA and N. TOTSUKA, *Corr. Sci.* **44**(10) (2002) 2333.
4. C. M. SUH, J. J. LEE and Y. G. KANG, *Fatigue Fract. Engng. Mater. Struct.* **13**(5) (1990) 487.
5. C. M. SUH, J. J. LEE, Y. G. KANG, H. J. AHN and B. C. WOO, *ibid.* **15**(7) (1992) 671.
6. A. BATAILLE and T. MAGNIN, *Acta Metallurgica et Materialia* **42**(10) (1994) 3817.
7. Y.-Z. WANG, K. EBTEHAJ, D. HARDIE and R. N. PARKINS, *Corr. Sci.* **37**(11) (1995a) 1651.
8. *Idem.*, *ibid.* **37**(11) (1995c) 1705.
9. *Idem.*, *ibid.* **37**(11) (1995b) 1677.
10. Y. OCHI, A. ISHII and S. K. SASAKI, *Fatigue Fract. Engng. Mater. Struct.* **8**(4) (1985) 327.
11. J. STOLARZ, *Mater. Sci. Engng. A* **234–236** (1997) 861.
12. G. SANTARINI, "Corrosion-Deformations Interactions, CDI'96. 1997," The Institute of Materials, Londres.
13. B. BUDIANSKY and R. J. O'CONNELL, *Intern. J. Solids Struct.* **12** (1976) 81.
14. A. HOENIG, *ibid.* **15** (1979) 137.
15. Z. HASHIN, *J. Mech. Phys. Solids* **36**(6) (1988) 719.
16. H. DENG and H. NEMAT-NASER, *Mech. Mater.* **13** (1992) 15.
17. Y. BENVENISTE, *Mech. Res. Commun.* **13**(4) (1986) 193.
18. F. CARVALHO and J. LABUZ, *Intern. J. Solids Struct.* **33**(28) (1996) 4119.
19. C. M. LIAO, J. M. OLIVE, M. GAO and R. P. WEI, *Corrosion* **54**(6) (1998) 451.
20. I. TSUKROV and M. KACHANOV, *Intern. J. Solids Struct.* **37**(41) (2000) 5919.
21. C. PEYRAT, O. RAQUET, M. HELIE and G. SANTARINI, *Annales de Chimie Sci. des Matériaux* **24**(4/5) (1999) 281.

Received 29 July 2003
and accepted 17 November 2004